arXiv:1610.07853v1 [cond-mat.mes-hall] 25 Oct 2016

Spin spirals in ultra-thin films driven by frustration of exchange interactions: Rh/Fe/Ir(111)

Niklas Romming[1,*], Markus Hoffmann[2,3], Bertrand Dupé[2], Kirsten von Bergmann[1], Stephan von Malottki[2], André Kubetzka[1], Roland Wiesendanger[1], and Stefan Heinze[2]

[1]Department of Physics, University of Hamburg, 20355 Hamburg, Germany
[2]Institute of Theoretical Physics and Astrophysics, Christian-Albrechts-Universität zu Kiel, 24098 Kiel, Germany
[3]Peter Grünberg Institut and Institute for Advanced Simulation, Forschungszentrum Jülich and JARA, 52425 Jülich, Germany
[*]nromming@physnet.uni-hamburg.de

ABSTRACT

Numerous complex non-collinear spin structures such as spin spirals and skyrmions have been observed recently in ultrathin transition-metal films at surfaces. In these systems the interfacial Dzyaloshinskii-Moriya interaction (DMI) plays a decisive role for the non-collinearity. Here, we demonstrate by density functional theory (DFT) and spin-polarized scanning tunneling microscopy (SP-STM) the occurrence of a spin spiral state which, in contrast, is induced by the frustration of exchange interactions. The DMI further stabilizes right rotating cycloidal spirals, however, the energy gain is small compared to that from the exchange. STM images reveal pseudomorphic growth of single atomic Rh layers on an atomic Fe layer on Ir(111) and show a stripe pattern with periods of 1.5 nm and 1.1 nm for the face-centered cubic (fcc) and hexagonal close-packed (hcp) Rh stacking, respectively, in very good agreement with the spin spiral periods obtained from DFT. For the fcc Rh stacking the spin spirals run along the $\langle 11\bar{2} \rangle$ directions, whereas for the hcp stacking the propagation direction of the spin spiral is tilted by an angle of about $\pm 10^\circ$ from this high-symmetry direction. Spin dynamics simulations show that magnetic fields of about 50 T are required to stabilize a hexagonal lattice of nanoscale skyrmions.

Dated: October 26, 2016

Introduction

Recently, it has been discovered that the DMI[1–3] plays an essential role, not only in bulk systems with broken inversion symmetry[4–6] but also at transition-metal surfaces and interfaces and can induce complex non-collinear spin structures with a unique rotational sense[7] such as cycloidal spin spirals[8–10], Néel type domain walls[11–16], as well as skyrmions and skyrmion lattices[17–26]. Spin-polarized scanning tunneling microscopy (SP-STM)[27] has allowed to reveal chiral domain walls, spin spirals and skyrmions at the atomic scale in ultra-thin films[7–11,13,17–19,26,28]. The emergence of spin spirals and skyrmions in such systems was explained by first-principles electronic structure theory based on density functional theory (DFT)[8,9,12,17,29,30]. In particular, a nanoskyrmion lattice was observed for the fcc Fe monolayer on Ir(111) and it was shown that for Pd/Fe bilayers on Ir(111) a spin spiral ground state driven by the DMI occurs, which can be turned into skyrmions in an applied magnetic field. These discoveries have established a new class of materials for skyrmions, i.e. ultra-thin transition-metal films. Such systems are very promising for future applications in spintronics[6,31,32] as it has been shown that skyrmions at such interfaces can be engineered either due to tuning of the DMI[24,33], the magnetocrystalline anisotropy[33] or the exchange interaction[20,34–36]. These approaches allow room temperature skyrmions in transition-metal multilayers[20,21,23–25] and current-driven skyrmion motion has been reported[21,25].

Here, we study the magnetic properties and magnetic interactions of a Rh/Fe bilayer on the Ir(111) surface. We find a spin spiral ground state which – in contrast to Pd/Fe/Ir(111) – is driven by frustration of exchange interactions and not DMI as shown by DFT calculations. Experiments employing SP-STM[27] reveal spin spiral states with periods of 1.5 nm and 1.1 nm for fcc and hcp stacking of the Rh overlayer, respectively, which are in good agreement with the DFT results. From the calculations we demonstrate that the hybridization at the Fe/4*d* interface leads to a small nearest-neighbor ferromagnetic exchange interaction which competes with a number of antiferromagnetic interactions beyond nearest neighbors. This frustration of exchange interactions is the driving force behind the spin spiral formation leading to a deep energy minimum in the energy dispersion. The DMI is a small effect in terms of the energy gain. However, it imposes a unique rotational sense onto the spin spirals and ensures their cycloidal character.

For fcc stacking of the Rh overlayer, we find experimentally that the spin spirals propagate along the $\langle 11\bar{2} \rangle$ high symmetry directions in agreement with the energy minima along the $\bar{\Gamma}-\bar{\mathrm{M}}$ directions found by DFT. For the hcp stacking, an analysis of SP-STM images and maps based on the tunneling anisotropic magnetoresistance (TAMR)[37,38] reveals that the spin spiral direction is tilted by about $\pm 10^{\circ}$ from this high symmetry direction. The energy landscape of spin spirals within DFT possesses an isotropic ring shape with shallow minima on the order of 0.2 meV. Therefore, small energy contributions may lead to the observed tilting off the high symmetry direction. We show that in principle Ruderman–Kittel–Kasuya–Yosida (RKKY)-like long-range exchange interactions can explain the deviation of the spin spiral propagation direction from the high symmetry directions.

A comparison between Pd/Fe/Ir(111) and Rh/Fe/Ir(111) shows that in both systems the magnetic ground state is a cycloidal right-rotating spin spiral. However, the period is on the order of 6 to 7 nm for Pd/Fe/Ir(111) and 1.1 to 1.5 nm for Rh/Fe/Ir(111). This is consistent with our DFT calculations and can be explained by the significant reduction of the nearest-neighbor ferromagnetic exchange in Rh/Fe/Ir(111) while the magnetocrystalline anisotropy and the DMI which is mainly due to the Fe/Ir interface are of similar magnitude in both systems. From spin dynamics simulations based on a spin Hamiltonian parametrized from first-principles calculations we show that a hexagonal lattice of skyrmions with a diameter on the order of 1 nm may appear in Rh/Fe/Ir(111) at magnetic fields of about 50 T. While such large magnetic fields cannot be applied in a typical experimental setup they may be created by using the interlayer exchange coupling as proposed previously in Ref. 20, 34.

First-principles calculations

We have performed first-principles calculations based on density functional theory (DFT) in order to determine the structural, electronic and magnetic properties of atomic Rh/Fe bilayers on the Ir(111) surface (see methods for details). The energy differences for the two stackings of Rh and the relaxed interlayer distances are summarized in Table 1 in comparison to the values obtained previously for Pd/Fe/Ir(111)[29]. In the ferromagnetic state the magnetic moments for fcc (hcp) stacking of the Rh overlayer are 2.44 μ_B (2.32 μ_B) for the Fe atoms and 0.29 μ_B (0.24 μ_B) for the Rh atoms.

	Pd/Fe/Ir(111)		Rh/Fe/Ir(111)	
	fcc	hcp	fcc	hcp
ΔE	23.06	0.0	0.0	6.46
$d_{4\mathrm{d}-\mathrm{Fe}}$	2.02	2.02	1.97	1.97
$d_{\mathrm{Fe}-\mathrm{Ir}}$	2.06	2.06	2.07	2.06
$d_{\mathrm{Ir}-\mathrm{Ir}}$	2.19	2.19	2.24	2.24

Table 1. Energy difference ΔE (in meV/Fe atom) between fcc and hcp stacking of the 4d overlayer and relaxed interlayer distances d (in Å) for Pd/Fe and Rh/Fe bilayers on Ir(111) in both stackings of the Pd or Rh overlayer.

Spin spiral calculations

We start by discussing the energy dispersion $E(\mathbf{q})$ of flat spin spirals displayed in Fig. 1 obtained without taking spin-orbit coupling (SOC) into account. Spin spirals are characterized by a vector $\mathbf{q}$ along which the spiral propagates and the magnetic moment at the lattice site $\mathbf{R}_i$ is given by $\mathbf{M}_i = M(\cos(\mathbf{q}\mathbf{R}_i), \sin(\mathbf{q}\mathbf{R}_i), 0)$ where M is the magnitude of the magnetic moment. The spin spiral vector $\mathbf{q}$ is chosen along a high symmetry line of the two-dimensional (2D) Brillouin zone. The period of the spin spiral is given by $\lambda = 2\pi/|\mathbf{q}|$. High symmetry points lead to specific spin structures, e.g. the $\bar{\Gamma}$ point corresponds to the ferromagnetic (FM) state, the $\bar{\mathrm{M}}$ point corresponds to the row-wise antiferromagnetic (RW-AFM) state and the $\bar{\mathrm{K}}$ point to the Néel state.

In Fig. 1 the energy dispersion $E(\mathbf{q})$ is shown along the $\bar{\Gamma}-\bar{\mathrm{M}}$ direction for bilayers of Pd/Fe and Rh/Fe on Ir(111). For Pd/Fe/Ir(111)[29], the energy rises relatively slowly as we increase q starting from the FM state ($q = 0$) but the energy difference to the RW-AFM state ($\bar{\mathrm{M}}$) is on the order of 100 meV. There is also a dependence on the stacking of the Pd overlayer: for fcc stacking we find a very shallow energy minimum at $\lambda \approx 3.5$ nm, while for hcp stacking the FM state is lowest in energy. By fitting the energy dispersions to a Heisenberg model as in Ref. 29 (see methods) we can obtain the exchange constants J_i for the i-th nearest neighbor shell. As seen in the inset of Fig. 1 and in Table 2, J_1 is on the order of 13 to 15 meV for both stackings. For fcc stacking, both the 2nd and 3rd nearest-neighbor exchange is negative, denoting an antiferromagnetic coupling. This frustration of exchange interactions leads to the small energy minimum. For hcp stacking, the 2nd nearest neighbor exchange is slightly positive while the 3rd nearest neighbor exchange is relatively large and favours antiferromagnetic coupling.

For Rh/Fe/Ir(111) the energy dispersions are qualitatively different. The FM states are still lower than the RW-AFM states, however, the energy difference has decreased by about a factor of two. There are deep energy minima on the order of $10-15$ meV/Fe atom for spin spirals with periods of $\lambda \approx 1.2$ nm. As for Pd/Fe/Ir(111), the nearest-neighbor exchange

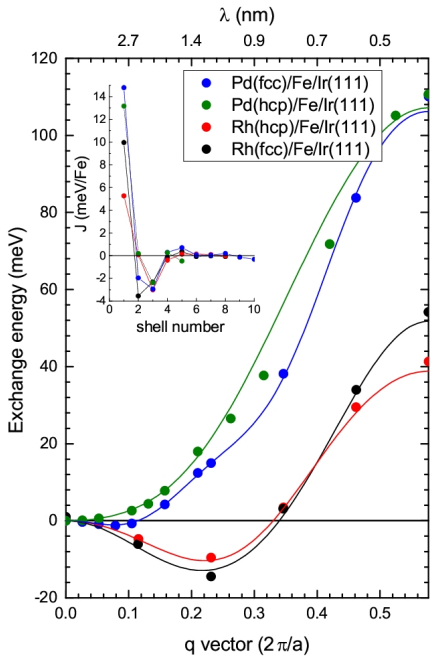

Figure 1. Energy dispersion of spin spirals along the $\bar{\Gamma} - \bar{\mathrm{M}}$ direction of the 2D-BZ for Pd/Fe/Ir(111) and Rh/Fe/Ir(111) in both fcc and hcp stackings of the Pd or Rh overlayer, respectively. Spin-orbit coupling has not been taken into account in these calculations. For Rh/Fe the magnetic exchange interaction stabilizes a spin-spiral of $\lambda \approx 1.2$ nm period. The inset shows the exchange constants extracted from fitting of energy dispersions along both high symmetry directions (cf. Table 2); the solid lines show the fit results.

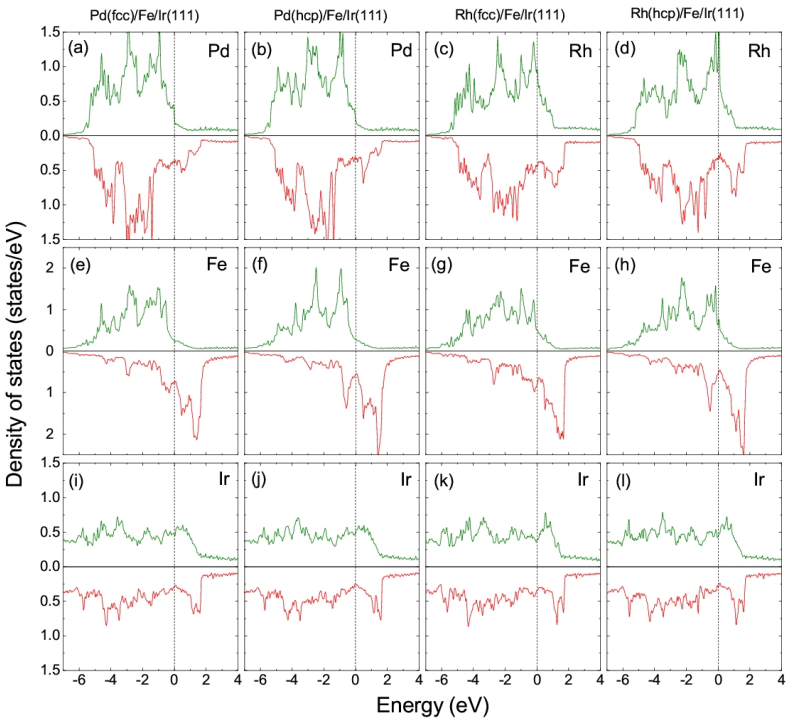

Figure 2. Spin-resolved local density of states for Pd/Fe/Ir(111) and Rh/Fe/Ir(111) in both fcc and hcp stackings. (a-d) Pd or Rh overlayer, as indicated, (e-h) Fe layer, (i-l) adjacent Ir layer. Green and red curves show the majority and minority spin channel, respectively.

interactions favour ferromagnetic coupling, but the values are reduced significantly, similar to the energy differences between the FM and the RW-AFM states (cf. inset of Fig. 1 and Table 2). The 2nd and 3rd nearest neighbor exchange interactions are of the same sign and of similar magnitude as for the respective stacking of the Pd overlayer. Mainly, the reduction of J_1 leads to an increased frustration of the exchange interactions, which triggers the spin spiral energy minima. Consequently, the spin spirals in Rh/Fe possess shorter periods than the ones in Pd/Fe.

	J_1	J_2	J_3	J_4	J_5	J_6	J_7	J_8	J_9	J_{10}
Pd(fcc)	14.73	−1.95	−2.88	0.32	0.69	0.01	0.01	0.13	−0.14	−0.28
Pd(hcp)	13.17	0.18	−2.38	0.26	−0.48					
Rh(fcc)	9.89	−3.72	−2.22	−0.00	0.26	−0.20	−0.02	−0.15	−0.14	0.26
Rh(hcp)	5.26	0.07	−3.00	−0.38	0.14	0.14	−0.09	−0.01		

Table 2. Exchange constants J_i to the i-th neighbor in the Fe film obtained from fitting the energy dispersion of homogeneous spin spirals calculated via DFT for Pd/Fe/Ir(111) and Rh/Fe/Ir(111) for fcc and hcp stacking of the 4d layer. The coefficients are given in meV/atom.

The modification of the exchange interaction can be understood based on the hybridization at the 4d/Fe interface. In Fig. 2 the local density of states is shown in the different atomic layers for Pd/Fe/Ir(111) and for Rh/Fe/Ir(111) in both stackings. As there is one electron less in the 4d-shell of Rh as compared to Pd, the Fermi energy E_F shifts into the 4d band and there are more states available at E_F. In consequence the hybridization in particular of the majority states of the Fe layer is modified significantly, leading to more majority states at E_F. This effect is very similar to what has been reported for Fe monolayers on different 4d- and 5d-transition-metal substrates[39]. Our calculations show that the exchange interaction can already be modified by single atomic layers of a 4d-transition-metal due to the change in the band filling and resulting hybridization with the Fe layer. This effect can be exploited to tune exchange interactions by alloying the 4d overlayer, e.g. Pd_xRh_{1-x}, such that skyrmions can be created as discussed recently for multilayers[35]. The hybridization between the Rh and Fe layer also depends on the stacking of the Rh layer as seen by comparison of Figs. 2c,g and d,h. Thereby, a fine tuning of the exchange interactions is possible, as can be seen in Table 2.

Dzyaloshinskii-Moriya interaction

In the last section we have shown that the exchange interactions in Rh/Fe/Ir(111) favour spin spiral states with periods of 1.2 nm. Due to the Fe/Ir interface, we also expect a significant DMI in these systems similar to that reported for Pd/Fe/Ir(111)[29,30]. We have therefore calculated the energy contribution due to spin-orbit coupling (SOC) for spin spirals in Rh/Fe/Ir(111) within first order perturbation theory[40,41]. As shown in Figs. 3a,b, SOC leads to a preference of right rotating cycloidal spin spirals for both types of stacking of the Rh overlayer. However, the energy differences are relatively small compared to the depths of the spin spiral energy minima neglecting SOC. Note, that the energy offset between the ferromagnetic state and spin spirals due to the magnetocrystalline anisotropy energy (MAE) has been taken into account (see dashed lines in Figs. 3a,b). The MAE amounts to 1.03 meV for fcc and 0.53 meV for hcp stacking and favours an out-of-plane magnetization direction for both.

The energy of spin spirals due to SOC, i.e. the contribution from the DMI, is on the order of a few meV as seen in Figs. 3c,d. Whereas the gain in energy due to DMI is relatively small compared to the exchange contribution, we still find a small shift of the spiral period from 1.2 to 1.3 nm for fcc Rh stacking and from 1.2 to 1.1 nm for hcp stacking. The rotational sense of the spin spirals is the same as for Pd/Fe/Ir(111) and the energy gain due to DMI is of similar magnitude. We obtain values of the DMI for nearest neighbors of $D_1 = 0.7$ meV and 0.85 meV and for the next-nearest neighbors of $D_2 = 0.16$ meV and -0.57 meV for fcc and hcp stacking of the Rh overlayer, respectively.

We find that the DMI depends sensitively on the Rh stacking, in particular the shape of the energy $\Delta E_{\mathrm{DM}}(\mathbf{q})$. The decomposition of the DMI energy into the contributions of the different atomic layers shows that the total DMI energy follows the Ir contribution. In the vicinity of $q = 0$, i.e. near the $\bar{\Gamma}$ point, the sign of the DMI energy from Ir differs for the two stackings. This shows that the hybridization with the Rh overlayer also influences the Fe/Ir interface. The contribution from the Rh layer is also non-negligible in this system. The sign of the DMI energy from the Rh layer also depends on the stacking of the overlayer. For hcp, the contributions of Ir, Fe and Rh are of similar size, and Ir and Rh are of the same sign. For fcc, the contribution from the Ir is generally stronger but the smaller contributions from Rh and Fe counteract against its strength.

Energy dispersion of spin spirals in the 2D Brillouin zone

So far, we have focussed on the energy dispersion of spin spirals along high symmetry directions of the two-dimensional Brillouin zone (2D BZ). As can be deduced from Fig. 3, for the hcp stacking of Rh the energy minima along the two high symmetry directions are nearly degenerate, whereas there is a clear energy difference between them for fcc stacking. To gain

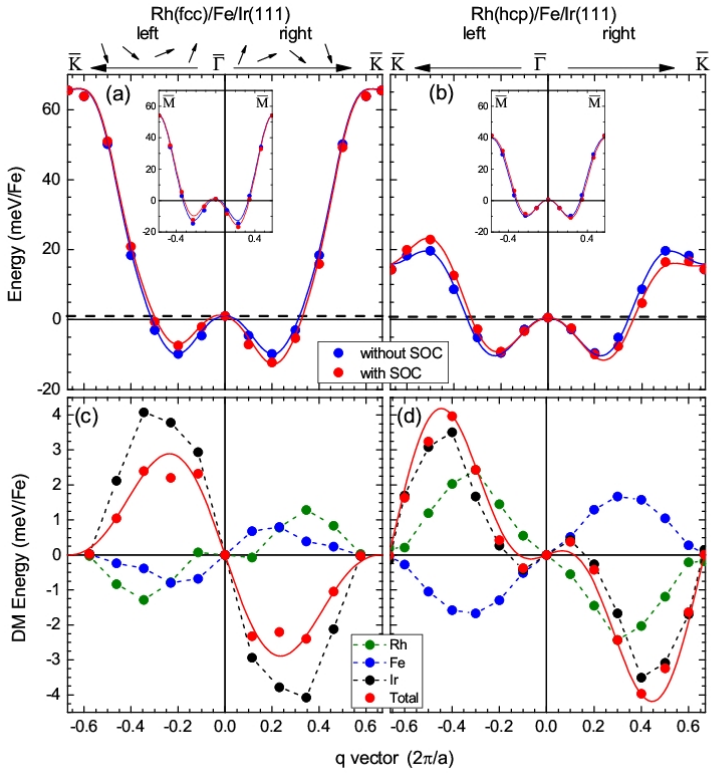

Figure 3. (a,b) Energy dispersion of left- and right-rotating cycloidal spin spirals along the $\bar{\Gamma}-\bar{\mathrm{K}}$ direction with and without spin-orbit coupling (SOC) for Rh/Fe/Ir(111) in fcc and hcp stacking, respectively. The offsets in energy (dashed lines) indicate the energy contribution from the magnetocrystalline anisotropy. Insets show the dispersion along the $\bar{\Gamma}-\bar{\mathrm{M}}$ direction. (c,d) Energy contribution to spin spirals due to the DMI. (Difference between curves in a,b.) The contributions are decomposed according to the Rh, Fe and Ir layers. The solid red line is the fit result to obtain the DMI values.

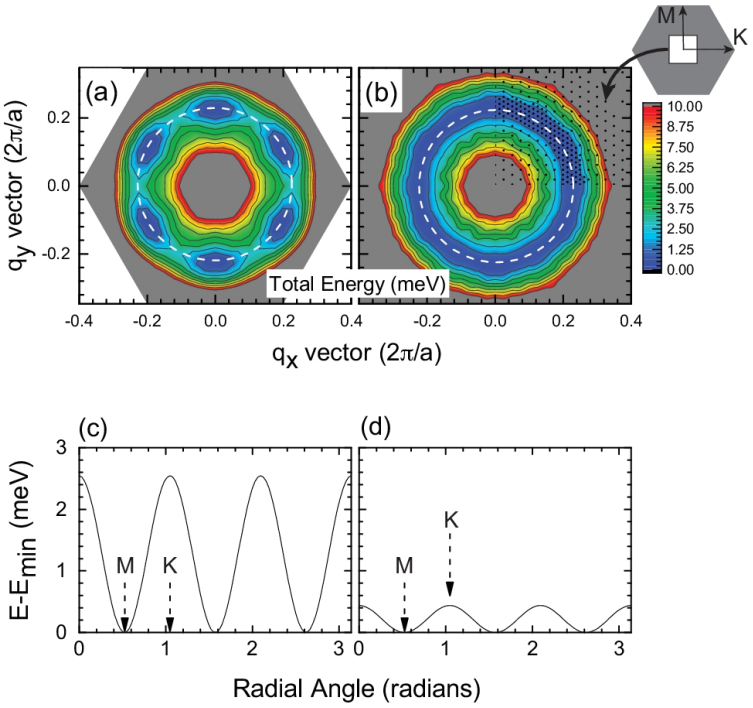

Figure 4. (a,b) Total energy of spin spirals including DMI for Rh/Fe/Ir(111) in fcc and hcp stacking in the vicinity of the $\bar{\Gamma}$ point of the 2D Brillouin zone as displayed in the inset in the upper right corner; black points in b show the positions of calculated energies. (c,d) energy along the dashed circle shown in panels (a,b), i.e. for spin spiral vectors in the range $q = 0.23 \pm 0.01 (2\pi/a)$ corresponding to a spin spiral pitch of 1.20 ± 0.05 nm.

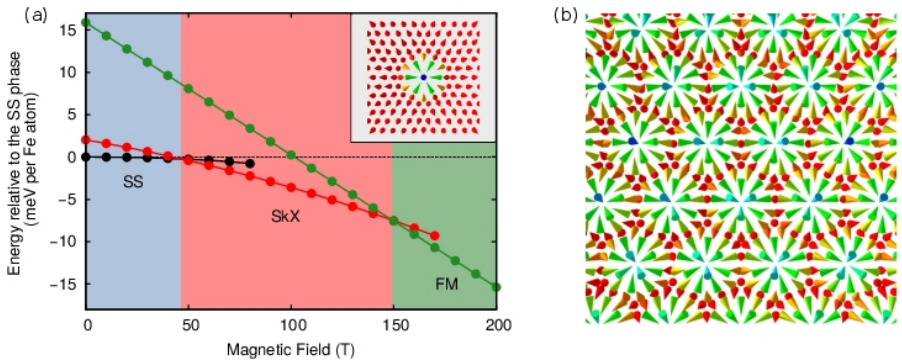

Figure 5. (a) Low temperature phase diagram of Rh/Fe/Ir(111) for fcc stacking of the Rh overlayer obtained by spin dynamics simulations based on the spin Hamiltonian parametrized from DFT calculations. Total energy per spin for the spin spiral (SS), skyrmion lattice (SkX) and ferromagnetic (FM) phase is shown by black, red, and green lines, respectively. Inset shows a metastable skyrmion at 180 T. (b) Hexagonal lattice of skyrmions with diameters of about 1 nm obtained for a magnetic field of 100 T. Every cone shows the spin of an Fe atom in the film. Red denotes upward and blue downward magnetization.

more knowledge about the dependence of the spin spiral energy on the propagation direction we need to consider the energy landscape of spin spirals in the full 2D BZ. We have performed spin spiral calculations for spiral vectors $\mathbf{q}$ in arbitrary directions. Since our calculations along the high symmetry directions have demonstrated that the energy minimum is located close to the $\bar{\Gamma}$ point, we focus on its vicinity (see inset of Fig. 4b). In Fig. 4a and b, the energy dispersion including DMI in the 2D BZ is given for fcc and hcp stacking of the Rh overlayer on Fe/Ir(111), respectively. For Rh(fcc)/Fe/Ir(111), we find six energy minima along the six equivalent $\bar{\Gamma}-\bar{\mathrm{M}}$ high symmetry directions. In contrast, there is a ring of nearly equal minimal energy for the hcp stacking of the Rh overlayer, see Fig. 4b. By plotting the energy along a ring at constant $|\mathbf{q}|$ as shown in Figs. 4c,d, we find that the energy minima for Rh(fcc)/Fe/Ir(111) are separated by barriers on the order of 2 meV, while for the hcp stacking the energy on the ring varies only on the order of about 0.2 meV. Therefore, we expect the spin spirals in Rh(fcc)/Fe/Ir(111) to propagate strictly along the $\bar{\Gamma}-\bar{\mathrm{M}}$ directions, whereas for hcp, the energy landscape that determines the propagation direction is nearly isotropic on the accuracy of our calculation.

Low temperature phase diagram

We have applied spin dynamics simulations (see methods for details) to determine the phase diagram of Rh/Fe/Ir(111) in an external magnetic field using the spin Hamiltonian parametrized based on the coefficients for the exchange interaction, the DMI, and the magnetocrystalline anisotropy obtained from our first-principles calculations. The phase diagram presented in Fig. 5a shows that the spin spiral state is favorable up to very large external magnetic fields of about 50 T applied perpendicular to the film. Between about 47 T and 149 T a hexagonal lattice of skyrmions with a diameter of about 1 nm is energetically preferred (cf. Fig. 5(b)). The skyrmions are of similar size as in the nanoskyrmion lattices of Fe/Ir(111)[17,28]. At even larger fields the ferromagnetic state is obtained. In the ferromagnetic phase, skyrmions with a diameter of about 1 nm can exist as metastable states (see inset of Fig. 5a).

STM experiments

We use (SP-)STM to characterize the growth, the stacking and the magnetism of Rh/Fe/Ir(111). Details on the sample preparation and measurement modes are given in the methods section.

Sample morphology

Figure 6a shows the topography and Fig. 6b a simultaneously recorded differential conductance ($\mathrm{d}I/\mathrm{d}U$)-map of a typical sample. At this bias voltage, the Fe and Ir have a similar $\mathrm{d}I/\mathrm{d}U$-signal. However, there are two clearly distinguishable contrast levels for the Rh islands on the Fe stripes, accompanied by triangular shapes either pointing up or down. This indicates pseudomorphic growth and the different levels are caused by the electronic difference due to the two possible stackings of the Rh. Their triangular and not hexagonal island shapes are caused by the two inequivalent types of edges ((001)-like and (111)-like), see inset of Fig. 6b. The two edge types possess different diffusion energies[42], which leads to a preference of one type of edge. As evident from the inset in Fig. 6b, straight island edges can be used to determine the crystallographic $\langle 1\bar{1}0\rangle$ directions (or close-packed rows (CPR)), which are marked by red lines in all following STM images. The fact that we observe both stackings with similar probability agrees with their small energy difference of 6 meV/Fe-atom, obtained from DFT (Table 1).

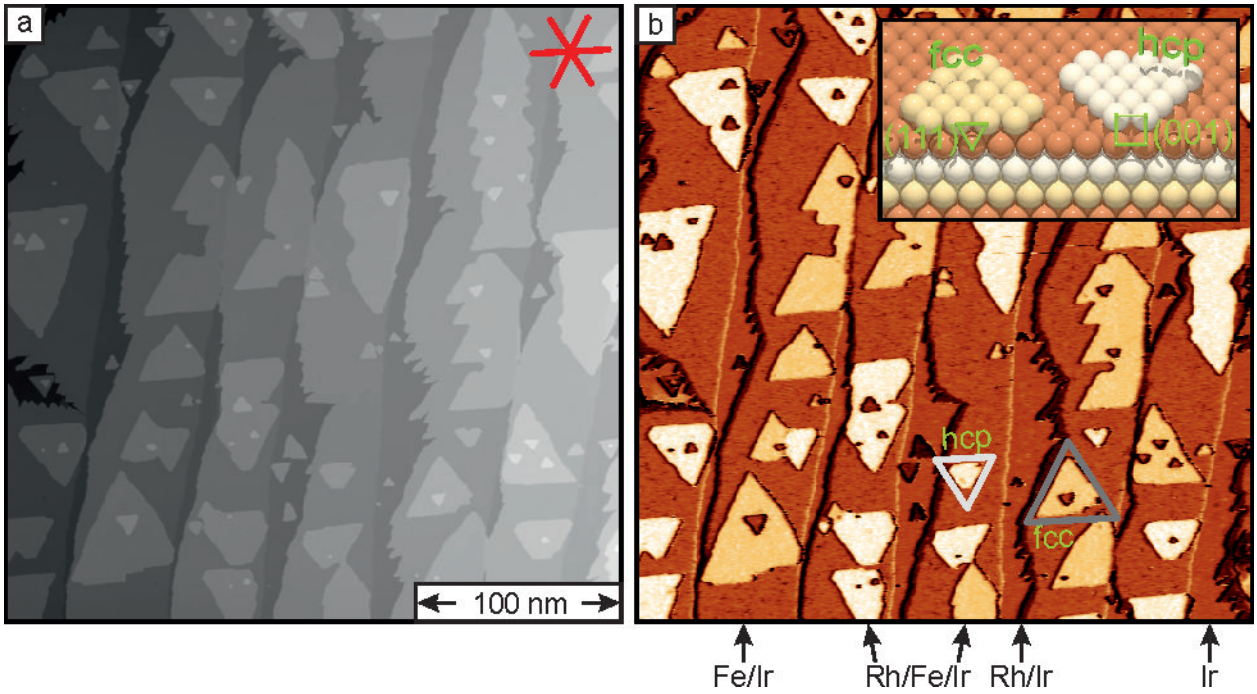

Figure 6. The stacking of Rh/Fe/Ir(111). (a) STM constant-current topography image of a typical Rh/Fe/Ir(111) sample with approx. 0.8 ML Fe and 0.4 ML Rh. Red lines mark the $\langle 1\bar{1}0 \rangle$ directions (or close-packed rows (CPR)), as obtained from straight island edges. (b) $\mathrm{d}I/\mathrm{d}U$-map recorded simultaneously to the image shown in a. Inset shows a ball model sketch of triangular Rh/Fe fcc and hcp islands. Different edge coordinations are indicated by the triangle and rectangle. ($U = +500$ mV, $I_{\mathrm{set}} = 750$ pA, $U_{\mathrm{mod}} = 50$ mV, $T = 8$ K).

To assign the stackings of Rh to either fcc or hcp, we have to consider island shapes and, since it was not possible to obtain atomic resolution on the Rh, make two assumptions. (i) We assume that the Rh connected to the Fe on the Ir surface continues the fcc stacking of the Fe. The same $\mathrm{d}I/\mathrm{d}U$-signal, as obtained for these fcc Rh stripes, is obtained on freestanding, up-pointing islands of Rh on Ir, which are thus also fcc. Down-pointing Rh/Ir islands with higher $\mathrm{d}I/\mathrm{d}U$-signal are hcp-stacked. (ii) The fcc (hcp) Rh islands on the Fe prefer the same type of edge as on the Ir and thus also point up (down). Based on these two assumptions, we conclude that the fcc (hcp) Rh/Fe/Ir(111) islands in Fig. 6b correspond to a lower (higher) $\mathrm{d}I/\mathrm{d}U$-signal. As will be shown later, this assignment is in agreement with results from DFT, regarding the magnetic states.

Magnetism of fcc Rh/Fe/Ir(111)

Figure 7a shows an SP-STM measurement of an fcc Rh/Fe/Ir(111) island with a cosine-like magnetic modulation with $\lambda_{\mathrm{fcc}} \approx 1.5$ nm period (Fig. 7b), which is a typical indication for homogeneous spin spirals, imaged with SP-STM[7,27]. As evident from the overview image (Fig. 7d), this modulation occurs in the three possible rotational domains with the propagation direction $\mathbf{q}$ strictly along the $\langle 11\bar{2} \rangle$ directions, which is consistent with the spin spiral energy minimum found along the $\bar{\Gamma} - \bar{\mathrm{M}}$ direction from DFT (cf. Fig. 4). The spin spirals are expected to be cycloidal due to the interface-induced DMI[7] (sketch in Fig. 7c). In Fig. 7d, we find different magnetic signal amplitudes for different propagation directions, which means the tip has an in-plane component[43]. It should be noted that there is an apparent correlation between the overall island shapes and the preferred propagation direction of the spin spirals along the longer direction of the islands, comparable to the preferred propagation direction of the spin spirals in Pd/Fe/Ir(111), possibly caused by a coupling to the island edges[18,44].

hcp Rh/Fe/Ir(111) with magnetic tip

Regarding hcp Rh/Fe/Ir(111) islands (Fig. 8) similar stripes with a slightly different period ($\lambda_{\mathrm{hcp}} \approx 1.1$ nm) are visible but it becomes directly evident that the magnetic structure differs from the one in fcc islands in several aspects: The propagation direction seems to be more flexible, is not strictly along the $\langle 11\bar{2} \rangle$ directions and varies locally. The nature of the periodic signal significantly differs from a cosine-like shape (profile in Fig. 8c). As also evident from the FFT of the data in Fig. 8b (inset), the image includes, in addition to the SP-STM signal (red dotted circles), a modulation in the same direction (yellow dotted circles), with half the period of the SP-STM signal. We interpret this as a TAMR signal as previously observed for cycloidal spin spirals[38]. Also, there are additional modulations visible in different directions (arrows) with a period of about

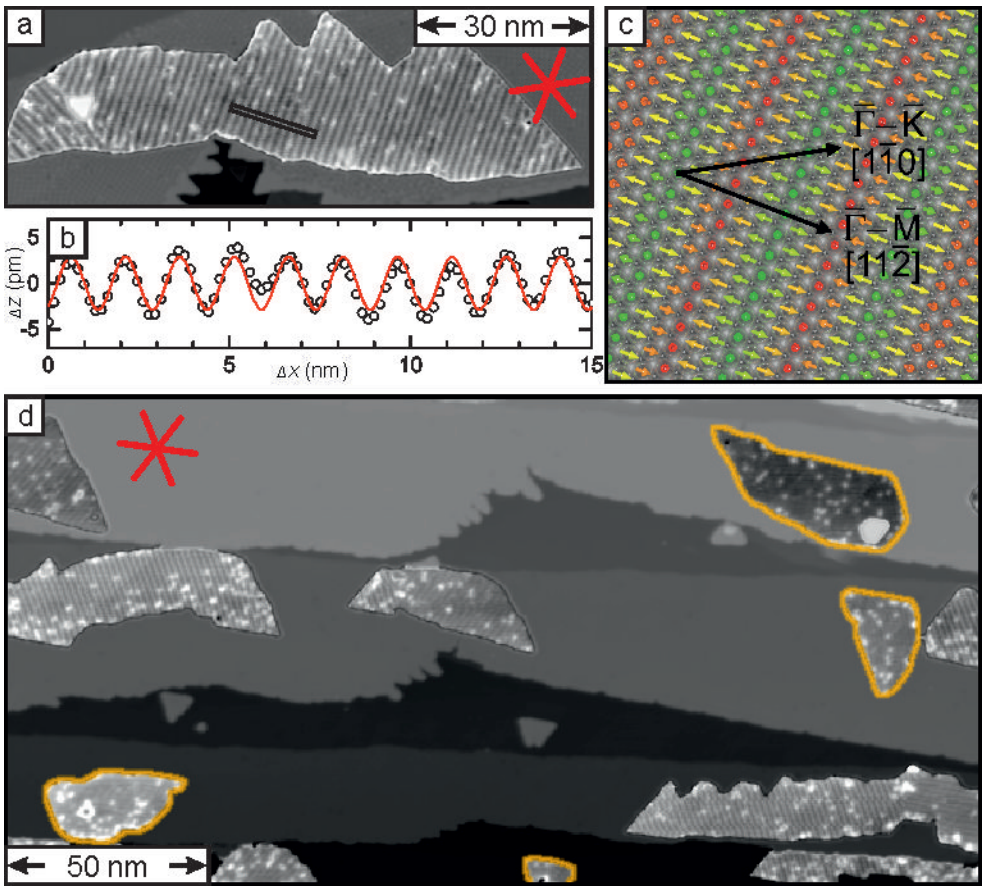

Figure 7. (a) SP-STM constant-current image of an fcc Rh/Fe/Ir(111)-island measured with a magnetic Cr-tip (contrast level adjusted locally to ± 20 pm). Red lines mark the $\langle 1\bar{1}0 \rangle$ directions (or CPR), as obtained from straight island edges ($T = 8$ K, $U = +30$ mV, $I_{\mathrm{set}} = 1.0$ nA). (b) Line profile along the rectangle in a. Solid line is a fit with a cosine-function as a guide to the eye. (c) Sketch of a homogeneous, cycloidal spin spiral with $\lambda_{\mathrm{fcc}} = 1.5$ nm along the $\bar{\Gamma} - \bar{\mathrm{M}}$ or $[11\bar{2}]$ direction. (d) SP-STM constant-current image with an in-plane magnetized Fe/W tip, contrast levels adjusted locally on the Rh/Fe/Ir(111)-islands to ± 20 pm, orange rims mark the hcp-islands. Red lines mark the $\langle 1\bar{1}0 \rangle$ directions (or CPR), as obtained from straight island edges ($T = 8$ K, $U = 600$ mV, $I_{\mathrm{set}} = 1.5$ nA).

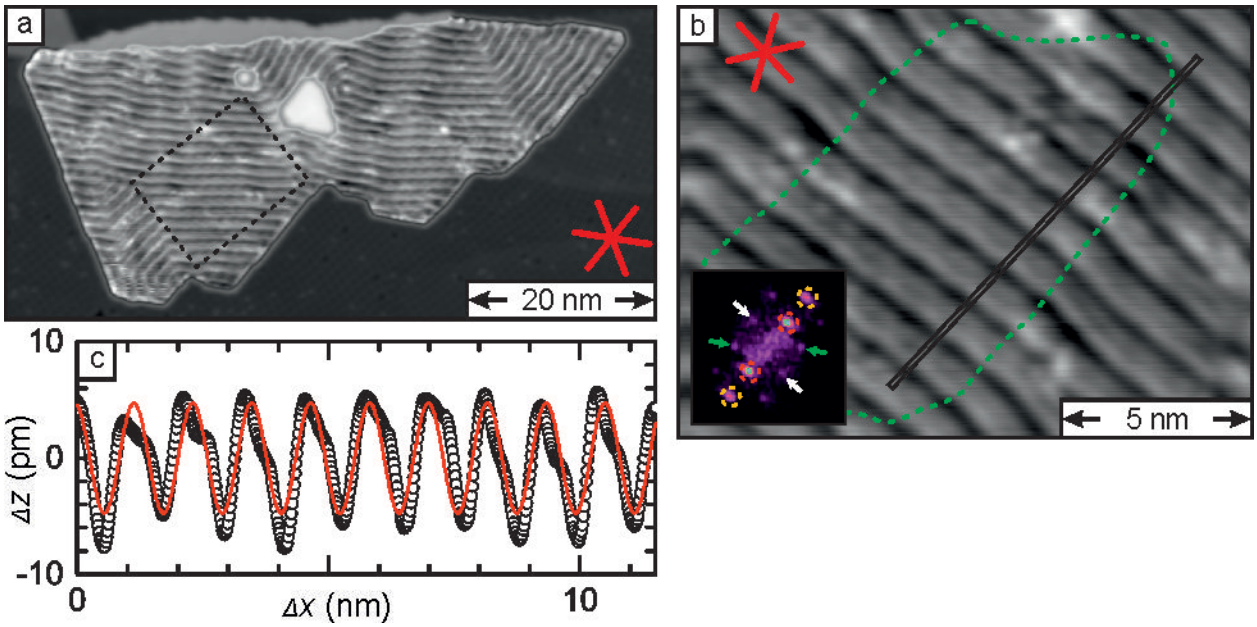

Figure 8. (a) SP-STM image of an hcp Rh/Fe/Ir(111)-island measured with out-of-plane magnetic Cr-tip (contrast level adjusted locally to ± 20 pm). (b) Zoom-in to the area marked by the dashed rectangle in a. The area enclosed by the green dotted line exhibits one singular tilted domain. Inset shows a 4 $\mathrm{nm}^{-1} \times 4\ \mathrm{nm}^{-1}$ cut-out of the FFT of the data in b. Red dotted circles mark spots caused by SP-STM contrast, yellow dotted circles mark spots caused by TAMR. Additional spots, indicated by arrows, correspond to a beating effect. Spots, marked by green arrows, are caused by the beating in the central domain, which is marked by the green dotted line, whereas the white arrows mark spots caused by beatings outside. (c) Line profile along the rectangle in b. Solid line is a fit with a cosine-function as a guide to the eye. Red lines in a,b mark the $\langle 1\bar{1}0 \rangle$ directions (or CPR), as obtained from straight island edges. ($T = 8$ K, a: $U = -30$ mV, $I_{\mathrm{set}} = 1.5$ nA; b: $U = -5$ mV, $I_{\mathrm{set}} = 3.0$ nA).

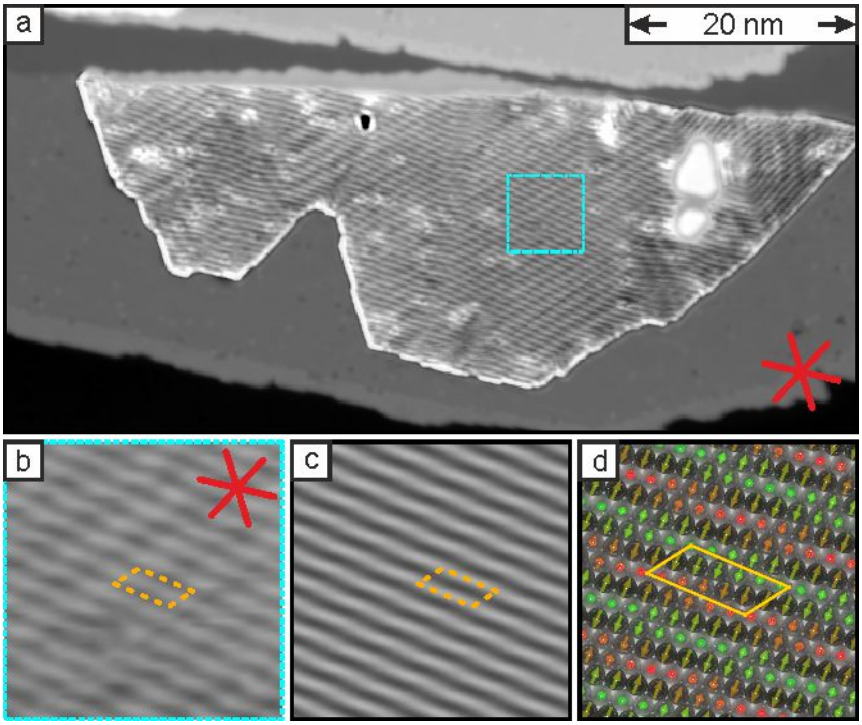

Figure 9. (a) Constant-current STM-image of hcp Rh/Fe/Ir(111) with a non-magnetic W-tip. Contrast level adjusted locally on the Rh/Fe/Ir(111)-island to ±15 pm ($T = 8$ K, $U = +30$ mV, $I_{set} = 1.5$ nA). (b) Cut-out (dotted square) of data shown in a. (c) STM-simulation of a homogeneous spin spiral with $\lambda_{hcp} = 4.0$ n.n.d and its propagation direction tilted $\alpha = +10°$ off the $[11\bar{2}]$ direction with the prefactor of the TAMR part of the signal being $\gamma = 0.1$ and a tip-sample distance $z_0 = 0.8$ nm. (d) Sketch of the magnetic structure, colorized according to the out-of-plane magnetization component. Sketch of the TAMR unit cell overlaid on the atomic lattice. Red lines in a,b mark the $\langle 1\bar{1}0 \rangle$ directions (or CPR), as obtained from straight island edges.

$\lambda_b = 1$ nm, which are so far unexplained. Regarding the preferred propagation direction with respect to the island shapes, there is a tendency for **q** to be roughly perpendicular to the long direction of hcp islands (observed also in several other islands, not shown) as opposed to the trend in the fcc islands. This suggests a different coupling of the magnetic structure to the island edges for the two stackings.

hcp Rh/Fe/Ir(111) with non-magnetic tip: TAMR Moiré pattern

To separate the non-spin-polarized from the spin-polarized part of the signal, we use a non-magnetic tungsten tip (see Fig. 9). As expected, the spin-polarized signal with $\lambda_{hcp} \approx 1.1$ nm vanishes but the shorter period with $\lambda_{TAMR} = \lambda_{hcp}/2 \approx 5.5$ Å remains, with the additional, up to now unexplained, modulation with $\lambda_b \approx 1$ nm in a different direction. We propose that this additional pattern is caused by a beating between the TAMR-contrast and the atomic lattice. Whenever periodic modulations of comparable, but not exactly the same, wavelengths interfere, Moiré patterns evolve[45]. It is clearly visible from Figs. 8 and 9 that the spin spirals do not propagate along the $\langle 11\bar{2} \rangle$ directions but rather at an angle of about ±10° off the $\langle 11\bar{2} \rangle$ directions (see Fig. 9b). To validate the hypothesis of a TAMR induced Moiré pattern, we performed an STM simulation based on the model described in Refs. 38,46 of a homogeneous cycloidal spin spiral with $\lambda_{hcp} = 4.0$ nearest neighbor distances (n.n.d = 2.715 nm) and its propagation direction tilted by $\alpha = +10°$ off the $[11\bar{2}]$ direction (Fig. 9d) with the prefactor of the TAMR part of the signal being $\gamma = 0.1$ and tip-sample distance $z_0 = 0.8$ nm. As evident from the simulation result (Fig. 9c), without any new assumptions, the experimental findings can be explained simply by a tilting of the spin spiral propagation direction away from a high-symmetry direction and an interference of the short-range TAMR-contrast with the atomic CPR.

This can be understood in more detail by taking some basic considerations about the TAMR signal with the atomic lattice into account. Figure 9d shows a sketch of the atomic lattice with the typical unit parallelogram from Fig. 9b,c on top. The red and green arrows show the locations of up or down spin direction for a homogeneous spin spiral, respectively. Since the TAMR signal is proportional to $\cos^2(\theta)$, with θ being the polar angle of the spin, and the TAMR is a local effect originating at the atom position, it becomes clear that the corners of the parallelogram are TAMR equivalent sites. In between, the spin up or

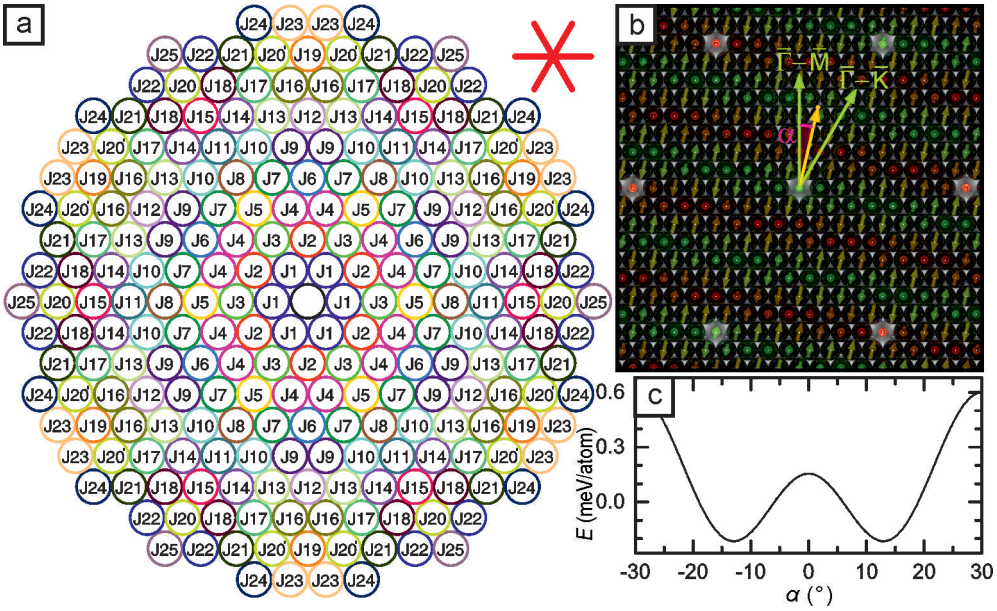

Figure 10. (a) Positions of J_i with respect to the central atom. Red lines mark the $\langle 1\bar{1}0 \rangle$ directions. (b) Sketch of the positions of spins corresponding to J_{25} (highlighted) of a spin spiral with $\lambda_{hcp} = 4.0$ n.n.d and $\alpha = +13°$ (**q** marked by orange arrow). (c) Direction dependence of the spin spiral energy $E_{SS,J_{25}}(\alpha)$ for $J_{25} = -0.1$ meV, $\lambda_{hcp} = 4.0$n.n.d, $0° \equiv \bar{\Gamma} - \bar{M}$ direction.

down positions do not coincide with equivalent atom positions and therefore result in a different TAMR signal and thus a Moiré pattern evolves. As Moiré patterns are known to be highly sensitive to small changes in angle or wavelength of the overlaid structures, they have been used in a variety of experimental techniques such as crystallography, metrology or optical alignment to obtain high-resolution data[47–49]. A close analysis of the Moiré pattern, represented by the unit parallelogram in Fig. 9b,c, also reveals a very sensitive dependence of its shape and size on the wavelength λ_{hcp} and the propagation direction determined by α. Therefore we can conclude from Fig. 9a, showing large domains with a singular Moiré pattern, that there must be some intrinsic interaction that forces the propagation direction of the spin spiral to a certain angle away from the high-symmetry directions. An analysis of several islands reveals a typical tilting of the propagation direction of $\alpha = \pm(9-12)°$ with respect to the $\langle 11\bar{2} \rangle$ directions and $\lambda_{hcp} = 3.90 - 4.15$ n.n.d. The spiral period is in good agreement with the DFT results and the tilting of **q** off the high symmetry directions is also compatible with, although not directly inferred by, the DFT calculations, i.e. the small energy barriers in Fig. 4.

Spin spiral propagation off high-symmetry directions

The propagation direction of a certain spin spiral with period λ is determined by the magnetic exchange interaction parameters. If only short-range interactions –short compared to λ– are taken into account, only energy minima along either $\bar{\Gamma} - \bar{M}$ or $\bar{\Gamma} - \bar{K}$ directions are possible. Long-range, indirect exchange interactions, such as e.g. the RKKY exchange[50–52], which are mediated by the conduction electrons, can also have an impact on the propagation direction of a spin spiral even generating local minima in between the high symmetry directions. It was shown that RKKY contributions to J_i may have a strong directionality, which is induced by the anisotropy of the underlying Fermi-surface[53], and that it can have a strength of roughly 0.1 meV for adatoms on surfaces for a distance on the order of 2 nm[54].

We use J_{25}, which acts between spins about 2.2 nm apart, as a simplified example to show how, in principle, a long-range exchange interaction of in our case $J_{i \gtrsim 15}$ could influence the propagation direction of the spin spiral in hcp Rh/Fe/Ir(111) and be responsible for the tilting of **q** away from high symmetry directions. Figure 10b depicts the locations of the spins that contribute to the energy of J_{25}, overlaid on the spin structure of a spin spiral with $\lambda_{hcp} = 4.0$ n.n.d at a propagation angle of $\alpha = 13°$. It becomes evident from the long distance to the involved spins compared to the spin spiral wavelength, that multiple relative spin orientations are possible when the propagation direction is rotated. And indeed, an analysis of the energy of this spin spiral as a function of the propagation direction for all $J_{i \neq 25} = 0$ and $J_{25} = -0.1$ meV (Fig. 10c) shows distinct local minima at $\alpha = \pm 13°$ of a few 100 μeV/atom. As seen from this simple exemplary calculation, a combination of weak non-isotropic long-range (compared to the spin spiral wavelength) interactions together with a rather isotropic energy landscape, as seen for hcp Rh/Fe/Ir(111) (see Fig. 4f), are a feasible explanation for the tilting of the propagation direction of the observed spin spiral state in hcp Rh/Fe/Ir(111).

Conclusions

Using SP-STM, we have observed spin spiral ground states in the ultrathin film system Rh/Fe/Ir(111) with periods of 1.5 nm and 1.1 nm for fcc and hcp stacking of the Rh layer, respectively. DFT calculations show that these spin spiral states are driven by the frustration of exchange interactions. The DMI leads to a small additional energy gain for right rotating cycloidal spin spirals. The spin spiral periods obtained from DFT are in good agreement with the experimental observations. The experiments show a distinct spin spiral propagation direction for fcc stacked Rh along the $\langle 11\bar{2}\rangle$ directions, which is supported by clear minima in the energy landscape of spin spirals in the full 2D BZ obtained by DFT. For hcp stacked Rh, an analysis of Moiré patterns caused by the TAMR and the atomic lattice shows that the propagation direction is tilted by $\pm 9-12^{\circ}$ with respect to the $\langle 11\bar{2}\rangle$ directions. We show that in principle long-range indirect exchange mechanisms can explain this effect.

In comparison to Pd/Fe/Ir(111), with a magnetic length-scale of about 7 nm and a significant contribution of the DMI to the ground state formation, the nearest-neighbor exchange constant for Rh/Fe/Ir(111) is significantly reduced, leading to the formation of an exchange-driven ~ 1.2 nm spin spiral ground state. The DMI, which is mainly due to the Fe/Ir interface, is of similar magnitude and sign in both systems. From spin dynamics simulations we also find a much larger critical magnetic field for skyrmion formation in the Rh/Fe system on the order of 50 T.This demonstrates the possibility to tune non-collinear systems in thin films not only by the interface-induced DMI, but in addition by the nearest-neighbor exchange interaction, which is also sensitive to interfaces.

Methods

Computational details

We used the full-potential augmented plane wave (FLAPW) method as implemented in the FLEUR code[55]. Symmetric films composed of 5 layers of Ir(111) with a Rh/Fe layer on each side were considered for the structural relaxation performed in the ferromagnetic state. The Fe layer has been chosen in the fcc stacking while for Rh both fcc and hcp stacking was considered. Both the Rh-Fe and the Fe-Ir distances were relaxed. The cutoff for the basis functions was $k_{\max} = 4.0$a.u.$^{-1}$ and 864 k-points in the full Brillouin zone (BZ) have been used. The muffin-tin radii of Rh, Fe and Ir have been chosen as 2.31 a.u., 2.23 a.u. and 2.31 a.u., respectively. For all calculations, we have used the equilibrium lattice parameter of Ir bulk relaxed within the local density approximation (LDA), i.e. 3.82 Å. Relaxations have been performed using the mixed LDA-GGA exchange-correlation potential as described in Ref. 56.

The energy dispersion of spin spirals[57] was obtained using the LDA exchange-correlation potential[58] for asymmetric films of Rh/Fe/Ir(111) with 5 Ir layers as for Pd/Fe/Ir(111) films[29]. We have used 1936 k-points in the full BZ and set $k_{\max} = 4.3 a.u.^{-1}$ to ensure convergence. The contribution to the spin spiral energy due to spin-orbit coupling (SOC) has been obtained in first-order perturbation theory[40,41].

The magnetocrystalline anisotropy energy (MAE), i.e. the total energy difference for a film with a magnetization pointing perpendicular to the surface and a film with a magnetization in the film plane, has been determined by self-consistent calculations using 15 layers of the Ir(111) substrate. We have used 1936 k-points and a basis function cutoff of $k_{\max} = 4.3 a.u.^{-1}$.

In order to study the magnetic phase space in an external magnetic field, we apply the spin Hamiltonian

$$H = -\sum_{ij} J_{ij}(\mathbf{m}_i \cdot \mathbf{m}_j) - \sum_{ij} \mathbf{D}_{ij} \cdot (\mathbf{m}_i \times \mathbf{m}_j) - \sum_i K(m_i^z)^2 - \sum_i \mu_s \mathbf{B} \cdot \mathbf{m}_i \,, \tag{1}$$

which describes the magnetic interactions between the magnetic moments $\mathbf{M}_i$ of atoms at sites $\mathbf{R}_i$ where $\mathbf{m}_i = \mathbf{M}_i / M_i$. The parameters for the exchange interaction (J_{ij}), the DMI ($\mathbf{D}_{ij}$), the magnetic moments (μ_s) as well as an uniaxial magnetocrystalline anisotropy (K) were obtained from DFT (see main text). To calculate the energy differences between the spin spiral (SS), skyrmion lattice (SkX) and ferromagnetic phases (FM), we have relaxed a supercell composed of (100 x 100) spins by integrating the Landau-Lifshitz equation (LL) of spin dynamics:

$$\hbar \frac{d\mathbf{m}_i}{dt} = \frac{\partial H_i}{\partial \mathbf{m}_i} \times \mathbf{m}_i - \beta \left(\frac{\partial H_i}{\partial \mathbf{m}_i} \times \mathbf{m}_i \right) \times \mathbf{m}_i \tag{2}$$

where β is the damping term and $\frac{\partial H_i}{\partial \mathbf{m}_i}$ is the effective magnetic field created by exchange, DMI, anisotropy and external magnetic field as derived from the spin Hamiltonian. To achieve fast relaxation, we have used $\beta = 0.5$. We have carried out simulations on a timescale of several hundred picoseconds with a time step of 0.1 fs. The equation of motion was integrated with a semi-implicit integrator[59].

Experimental details

The samples investigated in this study were prepared in ultra high vacuum (UHV) ($p_{\text{base}} < 10^{-10}$mbar) in a multi-chamber UHV system[60]. The Ir(111) crystal was initially cleaned and depleted of carbon contamination by repeated annealing cycles

in an oxygen atmosphere of p_{O_2} in the range of 10^{-6} to 10^{-7} mbar. For a standard sample preparation, the crystal was first sputtered with Ar-ions ($U_{acc} = 800$ V at $p_{Ar} \approx 9 \times 10^{-5}$ mbar and a sputtering rate of around 3 ML/min) for approx. 10 min. Subsequently, the sample was annealed to about 1600 K for about 90 s to restore a smooth surface. After a transfer of the sample to the evaporation chamber, lasting about 5 min, submonolayer amounts of Fe were deposited by molecular beam epitaxy (MBE) onto the warm surface at around 0.6 ML/min, leading to self-organized step flow growth in the fcc stacking, continuing the Ir stacking[61]. To reduce effects of intermixing between Rh and Fe, the sample then cooled down for about 1 h before the deposition of about 0.4 ML of Rh at around 0.1 ML/min. Subsequently, the sample was transferred into a low temperature STM[60].

To detect structural and magnetic properties of surfaces, several measurement modes of the STM can be employed. To distinguish between different materials and also stackings of a given material, maps of the differential conductance (dI/dU) can be recorded, which show the voltage-dependent local density of states of the sample. SP-STM[27] can be employed by using a magnetic tip and accessing the local spin structure of a sample by the tunnel magnetoresistance (TMR), which is proportional to the projection of tip and sample spin direction. Another way to obtain information about the magnetic state, even with a non-magnetic tip, is to use the tunneling anisotropic magnetoresistance TAMR[37,38], which depends on the sample's local spin direction relative to a crystallographic quantization axis, or the non-collinear magnetoresistance (NCMR)[62], which scales with the local magnetization direction gradient.

References

1. Dzyaloshinskii, I. E. Thermodynamic theory of weak ferromagnetism in antiferromagnetic substances. *Sov. Phys. JETP* **5**, 1259–1262 (1957).
2. Moriya, T. Anisotropic superexchange interaction and weak ferromagnetism. *Phys. Rev.* **120**, 91–98 (1960).
3. Crépieux, A. & Lacroix, C. Dzyaloshinsky-Moriya interactions induced by symmetry breaking at a surface. *J. Magn. Magn. Mater.* **182**, 341 (1998).
4. Mühlbauer, S. *et al.* Skyrmion lattice in a chiral magnet. *Science* **323**, 915–919 (2009).
5. Yu, X. Z. *et al.* Real-space observation of a two-dimensional skyrmion crystal. *Nature* **465**, 901–904 (2010).
6. Nagaosa, N. & Tokura, Y. Topological properties and dynamics of magnetic skyrmions. *Nat. Nanotechnol.* **8**, 899–911 (2013).
7. von Bergmann, K., Kubetzka, A., Pietzsch, O. & Wiesendanger, R. Interface-induced chiral domain walls, spin spirals and skyrmions revealed by spin-polarized scanning tunneling microscopy. *J. Phys.: Condens. Matter* **26**, 394002 (2014).
8. Bode, M. *et al.* Chiral magnetic order at surfaces driven by inversion asymmetry. *Nature* **447**, 190–193 (2007).
9. Ferriani, P. *et al.* Atomic-scale spin spiral with a unique rotational sense: Mn monolayer on W(001). *Phys. Rev. Lett.* **101**, 027201 (2008).
10. Phark, S. H. *et al.* Reduced-dimensionality-induced helimagnetism in iron nanoislands. *Nat. Commun.* **5**, 5183 (2014).
11. Kubetzka, A., Pietzsch, O., Bode, M. & Wiesendanger, R. Spin-polarized scanning tunneling microscopy study of 360° walls in an external magnetic field . *Phys. Rev. B* **67**, 020401 (2003).
12. Heide, M., Bihlmayer, G. & Blügel, S. Dzyaloshinskii-Moriya interaction accounting for the orientation of magnetic domains in ultrathin films: Fe/W(110). *Phys. Rev. B* **78**, 140403 (2008).
13. Meckler, S. *et al.* Real-Space Observation of a Right-Rotating Inhomogeneous Cycloidal Spin Spiral by Spin-Polarized Scanning Tunneling Microscopy in a Triple Axes Vector Magnet. *Phys. Rev. Lett.* **103**, 157201 (2009).
14. Chen, G. *et al.* Novel Chiral Magnetic Domain Wall Structure in Fe/Ni/Cu(001) Films. *Phys. Rev. Lett.* **110**, 177204 (2013).
15. Emori, S., Bauer, U., Ahn, S., Martinez, E. & Beach, G. Current-driven dynamics of chiral ferromagnetic domain walls. *Nat. Mater.* **12**, 611 (2013).
16. Ryu, K., Thomas, L., Yang, S. & Parkin, S. Chiral spin torque at magnetic domain walls. *Nat. Nanotechnol.* **8**, 527 (2013).
17. Heinze, S. *et al.* Spontaneous atomic-scale magnetic skyrmion lattice in two dimensions. *Nat. Phys.* **7**, 713–718 (2011).
18. Romming, N. *et al.* Writing and Deleting Single Magnetic Skyrmions. *Science* **341**, 636–639 (2013).
19. Romming, N., Kubetzka, A., Hanneken, C., von Bergmann, K. & Wiesendanger, R. Field-dependent size and shape of single magnetic Skyrmions. *Phys. Rev. Lett.* **114**, 177203 (2015).

20. Chen, G., Mascaraque, A., N'Diaye, A. T. & Schmid, A. K. Room temperature skyrmion ground state stabilized through interlayer exchange coupling. *Appl. Phys. Lett.* **106**, 242404 (2015).

21. Jiang, W. *et al.* Blowing magnetic skyrmion bubbles. *Science* **349**, 283–286 (2015).

22. Hoffmann, M. *et al.* Topological orbital magnetization and emergent Hall effect of an atomic-scale spin lattice at a surface. *Phys. Rev. B* **92**, 020401(R) (2015).

23. Boulle, O. *et al.* Room-temperature chiral magnetic skyrmions in ultrathin magnetic nanostructures. *Nat. Nanotechnol.* **11**, 449–454 (2016).

24. Moreau-Luchaire, C. *et al.* Additive interfacial chiral interaction in multilayers for stabilization of small individual skyrmions at room temperature. *Nat. Nanotechnol.* **11**, 444 (2016).

25. Woo, S. *et al.* Observation of room-temperature magnetic skyrmions and their current-driven dynamics in ultrathin metallic ferromagnets. *Nat. Mater.* **15**, 501–506 (2016).

26. Wiesendanger, R. Nanoscale magnetic skyrmions in metallic films and multilayers: a new twist for spintronics. *Nat. Rev. Mat.* **1**, 16044 (2016).

27. Wiesendanger, R. Spin mapping at the nanoscale and atomic scale. *Rev. Mod. Phys.* **81**, 1495–1550 (2009).

28. von Bergmann, K., Menzel, M., Kubetzka, A. & Wiesendanger, R. Influence of the local atom configuration on a hexagonal skyrmion lattice. *Nano Letters* **15**, 3280–3285 (2015).

29. Dupé, B., Hoffmann, M., Paillard, C. & Heinze, S. Tailoring magnetic skyrmions in ultra-thin transition metal films. *Nat. Commun.* **5**, 4030 (2014).

30. Simon, E., Palotás, K., Rózsa, L., Udvardi, L. & Szunyogh, L. Formation of magnetic skyrmions with tunable properties in PdFe bilayer deposited on Ir(111). *Phys. Rev. B* **90**, 094410 (2014).

31. Fert, A., Cros, V. & Sampaio, J. Skyrmions on the track. *Nat. Nanotechnol.* **8**, 152–156 (2013).

32. Sampaio, J., Cros, V., Rohart, S., Thiaville, A. & Fert, A. Nucleation, stability and current-induced motion of isolated magnetic skyrmions in nanostructures. *Nat. Nanotechnol.* **8**, 839–844 (2013).

33. Soumyanarayanan, A. *et al.* Analogue Tuning of Magnetic Skyrmion Properties at Room Temperature in Ir / Fe / Co / Pt Multilayers. *arXiv* 1606.06034 (2016).

34. Nandy, A. K., Kiselev, N. S. & Blügel, S. Interlayer exchange coupling: A general scheme turning chiral magnets into magnetic multilayers carrying atomic-scale skyrmions. *Phys. Rev. Lett.* **116**, 177202 (2016).

35. Dupé, B., Bihlmayer, G., Böttcher, M., Blügel, S. & Heinze, S. Engineering skyrmions in transition-metal multilayers for spintronics. *Nat. Commun.* **7**, 11779 (2016).

36. Rósza, L. *et al.* Skyrmions with Attractive Interactions in an Ultrathin Magnetic Film. *Phys. Rev. Lett.* **117**, 157205 (2016).

37. Bode, M. *et al.* Magnetization-Direction-Dependent Local Electronic Structure Probed by Scanning Tunneling Spectroscopy. *Phys. Rev. Lett.* **89**, 237205 (2002).

38. von Bergmann, K. *et al.* Tunneling anisotropic magnetoresistance on the atomic scale. *Phys. Rev. B* **86**, 134422 (2012).

39. Hardrat, B. *et al.* Complex magnetism of iron monolayers on hexagonal transition metal surfaces from first principles. *Phys. Rev. B* **79**, 094411 (2009).

40. Heide, M., Bihlmayer, G. & Blügel, S. Describing Dzyaloshinskii-Moriya spirals from first principles. *Physica B: Condens. Matter* **404**, 2678–2683 (2009).

41. Zimmermann, B., Heide, M., Bihlmayer, G. & Blügel, S. First-principles analysis of a homochiral cycloidal magnetic structure in a monolayer Cr on W(110). *Phys. Rev. B* **90**, 115427 (2014).

42. Müller, M., Albe, K., Busse, C., Thoma, A. & Michely, T. Island shapes, island densities, and stacking-fault formation on Ir(111): Kinetic Monte Carlo simulations and experiments. *Phys. Rev. B* **71**, 075407 (2005).

43. Hsu, P. J. *et al.* Guiding Spin Spirals by Local Uniaxial Strain Relief. *Phys. Rev. Lett.* **116**, 017201 (2016).

44. Schmidt, L. *et al.* Symmetry breaking in spin spirals and skyrmions by in-plane and canted magnetic fields. *New Journal of Physics* **18**, 075007 (2016).

45. Oster, G. & Nishijima, Y. Moiré Patterns. *Sci. Am.* **208**, 54–63 (1963).

46. Heinze, S. Simulation of spin-polarized scanning tunneling microscopy images of nanoscale non-collinear magnetic structures. *Appl. Phys. A* **85**, 407–414 (2006).

47. Sciammarella, C. A. The moiré method—a review. *Experimental Mechanics* **22**, 418–433 (1982).

48. Reid, G. Moiré fringes in metrology. *Optics and Lasers in Engineering* **5**, 63–93 (1984).

49. Halioua, M. & Liu, H.-C. Optical three-dimensional sensing by phase measuring profilometry. *Optics and Lasers in Engineering* **11**, 185–215 (1989).

50. Ruderman, M. A. & Kittel, C. Indirect Exchange Coupling of Nuclear Magnetic Moments by Conduction Electrons. *Phys. Rev.* **96**, 99–102 (1954).

51. Kasuya, T. A Theory of Metallic Ferro- and Antiferromagnetism on Zener's Model. *Prog. Theor. Phys.* **16**, 45–57 (1956).

52. Yosida, K. Magnetic Properties of Cu-Mn Alloys. *Phys. Rev.* **106**, 893–898 (1957).

53. Zhou, L. *et al.* Strength and directionality of surface Ruderman-Kittel-Kasuya-Yosida interaction mapped on the atomic scale. *Nat. Phys.* **6**, 187–191 (2010).

54. Wiebe, J., Zhou, L. & Wiesendanger, R. Atomic magnetism revealed by spin-resolved scanning tunnelling spectroscopy. *J. Phys. D: Appl. Phys.* **44**, 464009 (2011).

55. www.flapw.de.

56. Baud, S., Ramseyer, C., Bihlmayer, G. & Blügel, S. Relaxation effects on the magnetism of decorated step edges: Co/Pt(664). *Phys. Rev. B* **73**, 104427 (2006).

57. Kurz, P., Förster, F., Nordström, L., Bihlmayer, G. & Blügel, S. Ab initio treatment of noncollinear magnets with the full-potential linearized augmented plane wave method. *Phys. Rev. B* **69**, 024415 (2004).

58. Vosko, S. H., Wilk, L. & Nusair, M. Accurate spin-dependent electron liquid correlation energies for local spin density calculations: a critical analysis. *Can. J. Phys.* **58**, 1200–1211 (1980).

59. Mentink, J. H., Tretyakov, M. V., Fasolino, A., Katsnelson, M. I. & Rasing, T. Stable and fast semi-implicit integration of the stochastic landau-lifshitz equation. *J. Phys. C* **22**, 176001 (2010).

60. Pietzsch, O., Kubetzka, A., Haude, D., Bode, M. & Wiesendanger, R. A low-temperature ultrahigh vacuum scanning tunneling microscope with a split-coil magnet and a rotary motion stepper motor for high spatial resolution studies of surface magnetism. *Rev. Sci. Instrum.* **71**, 424–430 (2000).

61. von Bergmann, K. *et al.* Observation of a complex nanoscale magnetic structure in a hexagonal Fe monolayer. *Phys. Rev. Lett.* **96**, 167203 (2006).

62. Hanneken, C. *et al.* Electrical detection of magnetic skyrmions by tunnelling non-collinear magnetoresistance. *Nat. Nanotechnol.* **10**, 1039–1042 (2015).

Acknowledgements

We thank J. Wiebe for discussions. Research leading to these results has received funding from the Deutsche Forschungsgemeinschaft via project DU1489/2-1 and SFB668-A8. We gratefully acknowledge computing time at the supercomputer of the North-German Supercomputing Alliance (HLRN). This project has received funding from the European Union's Horizon 2020 research and innovation programme under grant agreement No 665095 (FET-Open project MAGicSky).

Author contributions statement

M.H. and B.D. performed the DFT calculations. S.v.M. performed the spin dynamics simulations. M.H., B.D., S.v.M. and S.H. analyzed and discussed the results from DFT and spin dynamics. N.R. performed the experiments and analyzed the data. A.K. made the STM simulations. N.R. and A.K. devised the model presented in Fig. 10. N.R., A.K., K.v.B., and R.W. discussed the experimental results. S.H. and N.R. wrote the manuscript. All authors reviewed the manuscript.

Additional information

The authors declare no competing financial interests.